American Journal of Nanotechnology & Nanomedicine

Research Article

Multifunctional Core/Shell Hybrid Fe_3O_4@ TiO_2@ZIF-8 Nanoparticles as a pH-responsive Vehicle Advances in Targeted Cancer Therapeutics - ∂

Minchao Liu[1,2#], Yuna Qian[1#], Zaian Deng[1], Ping Zhao[2*] and Jianliang Shen[1,3*]

[1]*School of Ophthalmology & Optometry, School of Biomedical Engineering, Wenzhou Medical University, Wenzhou, 325035, China*

[2]*School of Chemistry and Chemical Engineering, Guangdong Pharmaceutical University, Education Mega Centre, Guangzhou, 510006, China*

[3]*Wenzhou Institute of Biomaterials and Engineering, Chinese Academy of Science, Wenzhou, 325001, China*

[#]*These authors contributed equally to this work*

***Address for Correspondence:** Jianliang Shen, School of Ophthalmology & Optometry, School of Biomedical Engineering, Wenzhou Medical University, Wenzhou, 325035, China, Tel: +861-315-737-2733; ORCID: orcid.org/0000-0003-4351-4872; E-mail: shenjl@wibe.ac.cn

Ping Zhao, School of Chem istry and Chemical Engineering, Guangdong Pharmaceutical University, Education Mega Centre, Guangzhou, 510006, China, E-mail: zhaoping666@163.com

Submitted: 27 April 2018 **Approved:** 14 June 2018 **Published:** 16 June 2018

Cite this article: Liu M, Qian Y, Deng Z, Zhao P, Shen J. Multifunctional Core/Shell Hybrid Fe_3O_4@ TiO_2@ZIF-8 Nanoparticles as a pH-responsive Vehicle Advances in Targeted Cancer Therapeutics. Am J Nanotechnol Nanomed. 2018; 1(1): 016-027.

ABSTRACT

It is widely accepted that an ideal targeted drug delivery system would be directed to the tumor tissue and selectively release therapeutic molecules. In this study, we have developed a ZIF-8 coated magnetic nano delivery system named Fe_3O_4@TiO_2@ZIF-8. Because of the Fe_3O_4 magnetic core, the drug delivery vehicle provides targeting of drugs to the tumor site under a magnetic field. Owing to the porosity and acid-sensitivity of zeolitic imidazolate framework-8 (ZIF-8), Fe_3O_4@TiO_2@ZIF-8 NPs not only displayed an improved drug loading capacity compared to most of the inorganic nanocarriers, but also exhibited excellent pH-triggered release of Daunomycin (DNM) *in vitro*. Co-incubation of Hela cells with hybrid NPs shows low toxicity and rapid cellular endocytosis, consequently displays enhanced the inhibition of cancer cell growth by DNM. These results provide convincing evidence establishing the multifunctional Fe_3O_4@ TiO_2@ZIF-8 NPs as promising candidates for tumor therapy.

Keywords: Daunomycin; Superparamagnetic iron oxide nanoparticle; Magnetic targeted drug delivery; Zeolitic imidazolate framework-8; pH-triggered release

INTRODUCTION

Cancer has become a leading cause of death in the past decades. However, current anticancer chemotherapies have several drawbacks including limited solubility, reduced bioavailability, drug resistance, systemic toxicity and a poor nonselective bio-distribution [1-3]. Therefore, there is an urgent need to develop novel anticancer drugs with new modes of action that can selectively target cancer cells while sparing normal cells of the host. Up to date, a number of magnetic nanoparticles have been designed for the purpose of Magnetic Resonance Imaging (MRI), targeted drug delivery, magnetic enrichment and purification [4-6]. Among them, the Superparamagnetic Iron Oxide Nanoparticles (SPION) are remarkable since they are devoid of magnetic remanence due to their small size. Furthermore, magnetic nanoparticles can be used as core to construct core-shell structure, which allow the single nanocomposite to exert multifunctions including drug delivery, therapy and imaging [7,8]. Daunorubicin (DNM) and Doxorubicin (DOX) are member of the anthracycline family, there are too few people who study daunorubicin as a model drug, while there are many people who study doxorubicin as a model drug. They has been frequently reported to be loaded on the SPION [9-11].

TiO_2 nanoparticle is a potential dynamic therapy agent in cancer therapy due to its excellent biocompatibility and unique photocatalytic properties [12,13]. Recently, our group has synthesized multifunctional Fe_3O_4@TiO_2 nanocomposite for potential applications in both magnetic resonance imaging (Fe_3O_4 constituent) and inorganic photodynamic therapy (TiO_2 constituent) [14]. However, the drug loading of Fe_3O_4@TiO_2 nanocomposite attributed to the electrostatic interaction between the cationic DNM and the negatively charged surface of Fe_3O_4@TiO_2. As is well known, both stable drug loading in physical serum and selective drug release at intracellular target sites are very significant for a drug vehicle. The electrostatic interaction could not bring high payload or sensitive drug release in tumor microenvironment.

To resolve the problems above mentioned, Metal Organic Frameworks (MOF) materials are employed in this study. MOF are a class of porous hybrid materials with defined cage structure, their assembly and functionalization recently have captivated much attention because of their intriguing structures and potential applications in gas storage [15,16], gas sensing [17,18], chromatographic separation [19,20], heterogeneous catalysis [21,22] and many other [23,24]. In particular, zeolitic imidazolate framework-8 has exhibited the desired characteristic of pH-sensitivity as a drug storage and delivery vehicle in terms of the tumor microenvironment. Furthermore, ZIF-8 is formed by 2-methyl imidazolate and zinc ions, which are components of physiological systems, where by zinc is the second most abundant transition metal in biology, and the imidazole group is integral to the amino acid, histidine. The coordination between the zinc and imidazolate ions dissociates at pH 5.0-6.0, which makes the drug release pH responsive and optimal for targeting cancer cells where extracellular microenvironments (pH 5.7-7.8) are more acidic than healthy tissues [25-27]. Sun has demonstrated that ZIF-8 is a valuable candidate as a pH-sensitive drug delivery vehicle for the first time [28]. Wu has reported the successful fabrication of MOFs encapsulating superparamagnetic g-Fe_2O_3 inside their porous frameworks [29].

In this study, a novel active tumor-targeting system (Fe_3O_4@ TiO_2@ZIF8-DNM NPs) was designed by Core/Shell Hybrid nanoparticles (Fe_3O_4@TiO_2@ZIF8 NPs) as carrier and DNM as the model of antitumor drug. Apart from providing stability to NPs, the key attribute of Fe_3O_4@TiO_2@ZIF8 NPs is their ability to enhance drug transport by effective passive targeting toward cancerous tissues and making sensitize the multi-drug resistance tumors to various anticancer agents. Moreover, the inner core of Fe_3O_4@ TiO_2 NPs functions as a bifunctional imaging agent, while the shell of ZIF-8 serves as a pH-responsive platform for drug delivery. The morphology and composition of the Fe_3O_4@TiO_2@ZIF-8-DNM NPs were characterized by FT-IR, TEM, UV, zeta potentials. Uterine cervix carcinoma is one of the most common malignant tumors which severely threatens women health and life. Uterine cervix carcinoma cell lines as the tumor cells were chosen to evaluate the antitumor potentiality of Fe_3O_4@TiO_2@ZIF-8-DNM NPs using in vitro drug release kinetics, cellular uptake, cytotoxicity and apoptosis experiments.

MATERIALS AND METHODS

General materials and reagents

Zinc nitrate hexahydrate ($Zn(NO_3)_2{\cdot}6H_2O$,Tetrabutyl Titanate (TBOT) were purchased from Aladdin Biochemical Technology Co, Ltd (China). 3-(4,5-Dimethylthiazol-2-yl)-2,5-diphenyltetrazolium bromide (MTT), Prussian Blue-Neutral Red Staining Kit and N,N-dimethyl-4-nitrosoaniline (RNO) were obtained from Sigma-Aldrich. All the other chemicals were of analytical grade, and Millipore water (18.2 MΩ) was used throughout the experiments.

Instrumentation

The Transmission Electron Microscope (TEM) analyses were performed with a JEM-2010HR transmission electron microscope. Size distribution of the particles was obtained on a Malvern Zetasizer

Nano ZS90 instrument (Malvern, UK). UV-Vis and FTIR spectra were recorded on a Shimadzu UV-3150 spectrophotometer and an Equinox 55 Fourier transformation infrared spectrometer, respectively. Fluorescence microscopy of apoptosis assays was performed with an OX31 fluorescence microscope (Olympus, Japan). Cell cycle analysis, annexin Vefluorescein isothiocyanate/Propidium Iodide (PI) assay of apoptotic cells and detection of mitochondrial membrane potential were performed with a FACS can flow cytometer (BD, USA).

Experimental methods

Preparation of Fe_3O_4@TiO_2@ZIF-8 NPs: Fe_3O_4 NPs were synthesized by a coprecipitation of ferric and ferrous chlorides in alkaline medium following the method we previously reported [30]. The Fe_3O_4@TiO_2 core-shell nanocomposites were fabricated via sol-gel process of hydrolysis and condensation of TBOT. Briefly, about 30 mg of Fe_3O_4 nanoparticles were dispersed in a mixed solvent containing 90 mL of ethanol and 30 mL of acetonitrile, and mixed with 0.5 mL of concentrated ammonia solution (0.30 mL, 28 wt%) under ultrasound for 15 min. Afterwards, 0.5 mL of TBOT was added to the above suspension under continuous mechanical stirring. After reacting for 1.5 h, the products were collected by magnetic separation and washed with ethanol for several times. Then, 15 mg of Fe_3O_4@TiO_2 nanospheres were added to a methanol solution containing 80 mg of $Zn(NO_3)_2 \cdot 6H_2O$ and 138 mg of 2-methylimidazolate. The entire reaction process was performed at 60°C for 1 h with agitated stirring. Then, the mixture was cooled to room temperature, and the resulting product was separated using a magnet and washed several times with methanol before drying in an oven at 60°C.

Drug loading and release study: A calculated amount of DNM was added to Fe_3O_4@TiO_2@ZIF-8 NPs dispersion, obtained as described above, resulting in a different DNM concentration in solution. The mixture of DNM and Fe_3O_4@TiO_2@ZIF-8 NPs dispersion was incubated for 24 h at room temperature and then centrifuged at 10,000 g for 15 min. The obtained pellet after centrifugation was separated from the supernatant solution and redispersed in deionized water prior to further characterization. The drug levels of the supernatant obtained were determined by UV spectrophotometer at 480 nm and the DNM loading content and entrapment efficiency were calculated by Eqs. (1) and (2) as follows, respectively. Triplicate samples were analyzed.

$$\text{Drug loading content}\left(\%, \frac{w}{w}\right) = \frac{\text{mass of drug in nanoparticles}}{\text{mass of nanoparticles recovered}} \times 100$$

$$\text{Drug entrapment efficiency}\left(\%, \frac{w}{w}\right) = \frac{\text{mass of drug in nanoparticles}}{\text{mass of drug used in formulation}} \times 100$$

The release of DNM from Fe_3O_4@TiO_2@ZIF-8 NPs was carried out both at physiological pH (≈7.4) and at lysosomal pH of cancer cells (≈5.6) at 37°C. The amount of DNM released was monitored spectrophotometrically at 480 nm and the amount of the released drug was calculated from a standard curve of free DNM solution.

***In vitro* cytotoxicity:** The biocompatibility of the Fe_3O_4@TiO_2@ZIF-8 NPs and the cytotoxicity of the free DNM and Fe_3O_4@TiO_2@ZIF-8-DNM NPs was assessed by using the MTT assay. For these studies, uterine cervix carcinoma cell line (Hela), the human lung adenocarcinoma cell line (A549) were provided by School of Pharmacy in Guangdong Pharmaceutical University with RPMI 1640 medium containing 10% Fetal Bovine Serum (FBS), and 100 U/mL penicillin and 100 U/mL streptomycin at 37°C in a humidified atmosphere with 5% CO_2. The cells (1×10^4 cells/well) were seeded into 96-well plates and incubated for 24 h, respectively. Then the Fe_3O_4@TiO_2@ZIF-8 NPs, Fe_3O_4@TiO_2@ZIF-8-DNM NPs and the free DNM with different concentration were added. After incubation for 48 h at 37°C, the culture medium was removed and 20 μL of MTT reagent (diluted in culture medium, 0.5 mg/mL) was added. Following incubation for 4 h, the MTT/medium was removed carefully and DMSO (150 μL) was added to each well for dissolving the formazan crystals. Absorbance of the colored solution was measured at 570 nm using a microplate reader (Bio-Rad, iMarkTM).

Prussian blue staining: HeLa cells were seeded on 24-well plates at a cell density of 1×10^4 cells per well and incubated overnight. A solution of the Fe_3O_4@TiO_2@ZIF-8 NPs magnetic nanospheres with a concentration of 50 μg/mL was then added and the cells were cultured for 6 h. After the end of the culture period, each well was washed three times with Phosphate Buffered Saline (PBS), treated with 4% paraformaldehyde solution at 4°C for 30 min to fix the cells, and washed three times with PBS again. A 1:1 mixture of 5% potassium ferrocyanide (II) trihydrate solution and 5% HCl was added to each well and the cells were incubated at room temperature for 1 h before being counterstained with neutral red. Each well was then washed three times with PBS and analyzed by light microscopy.

Cell migration inhibition study by scratch wound assay: To determine if quantifiable cell migration occurred after Fe_3O_4@TiO_2@ZIF-8-DNM NPs treatment, *in vitro* scratch assays were performed. HeLa cells were seeded in 6 well plates and when cells reached a confluence of 95% wounds were made in cell culture using a tip. Culture medium was changed to remove loose cell debris, and a defined area of the wound was photographed under an inverted microscope for a total period of 48 h.

Magnetic targeting study: HeLa cells were seeded in a 60 mm petri dish and incubated overnight, and then a solution of the magnetic nanospheres with a concentration of 50 μg/mL was added. For magnetic targeting study, a magnet (about 4 T) was placed beside the petri dish. After incubation for 24 h, the petri dish was photographed and the cells in the position of magnet (targeting area) and the area with a much weaker magnetic field strength (control area) were observed using a light microscope.

Flow cytometry analysis of nanoparticle drug delivery efficiency: Fe_3O_4@TiO_2@ZIF-8-DNM drug delivery efficiency was characterized by flow cytometry using a BD FACSCalibur flow cytometer (Becton Dickinson Inc., USA). Briefly, Hela cells were seeded in 12 well culture plates with a total of 1×10^5 cells per well. Cells were grown for 24 h in the same conditions as previously described. Afterward, the cells were exposed to different formulations of Fe_3O_4@TiO_2@ZIF-8-DNM NPs during 12 h. Following incubation, the cells were extensively rinsed with PBS and harvested with 0.25% trypsin. For flow cytometry analysis, the cells were resuspended in fresh PBS. Data acquisition was performed in the Cell Quest software where 1×10^4 events were recorded in the Hela cells region. Data analysis was performed in the trial version of FlowJo software v. 10.0.6

Cell internalization: For cell internalization experiment, cells were seeded for 48 h in standard 24-well plates at 1×10^4 cells per well. Then the culture medium was discarded and the cells were treated for 12 h with 500 μL of medium containing Fe_3O_4@TiO_2@ZIF-8 NPs suspensions (0.5 μg/mL DNM). The fluorescence of DNM in the cells was observed with fluorescence microscope.

Cell cycle phase distribution and apoptosis assay: For the determination of cell cycle phase distribution of DNA content, Hela (5×10^4 cells/well) cells were seeded into 6-well recovery. Cells were treated with an inhibitory concentration (IC50) of Fe_3O_4@TiO_2@ZIF-8-DNM NPs for 48 h. Untreated cells (control) were also incorporated. After incubation, cells were harvested and fixed with ice-cold 70% ethanol (5 mL) at -20°C. They were allowed to stand overnight, and cell pellets were further processed using the FITC Annexin V Apoptosis Detection Kit (BD PharmingenTM) according to the manufacturer's protocol by Fluorescent Activated Cell Sorter (FACS) analysis (BD FACSVerse, NJ, USA) [31].

Percent apoptotic cell death was determined by flow cytometrically (FACS Calibur, BD Biosciences, CA, USA). The induction of apoptosis by free DNM and Fe_3O_4@TiO_2@ZIF-8-DNM NPs was studied by flow cytometry [32,33]. Briefly, Hela cells at a density of 3.0×10^5 cells/ml were grown in 25 cm^2 culture flasks containing 5 ml of growth medium in tripli-cates and incubated at 37°C in a humidified atmosphere (5% CO_2) for 12 h. Next day, 5 ml medium containing 0.5 µg/ml of native DNM and equivalent concentration of Fe_3O_4@TiO_2@ZIF-8-DNM NPs were added to the flasks and incubated in 5% CO_2 incubator. Cells treated with culture medium and culture medium containing Fe_3O_4@TiO_2@ZIF-8 NPs were used as control, respectively. Next day, each flask was washed three times with PBS, trypsinized with 0.25% trypsin and collected by centrifugation. The pelleted cells were resuspended in 400 µL of 1-binding buffer, 5 uL 1 mg/ml Annexin V-FITC, and incubated at room temperature in dark for 15 min. Afterwards, 10 µL 10 mg/ml propidium iodide was added and the mixture incubated in the dark for another 5 min. Stained cells were analyzed on flow cytometer (FACS Caliber; Bectone Dickinson, San Jose, CA) using Cell Quest software with a laser excitation wavelength at 488 nm. The apoptotic cells were determined by analyzing 10,000 ungated cells using a FACS can flow cytometer and Cell Quest software.

Trypan blue exclusion test: To determine the viable cell number, trypan blue exclusion test was performed. Cells were suspended in Phosphate Buffer Saline (PBS). A small sample (0.1 mL) of cells from single cell suspension was aseptically removed and mixed with 0.16% trypan blue (in PBS). Viable cells (the cells which were not intruded by trypan blue) were counted in hemocytometer.

RESULTS AND DISCUSSION

Synthesis and characterization

Figure 1 showed typical TEM image of Fe_3O_4@TiO_2@ZIF-8 particles. Based on microscopic image, the particles had approximately spherical morphology. Core/Shell Hybrid Fe_3O_4@TiO_2@ZIF-8 Nanoparticles could be seen in the TEM image where the core and the outer layer in particles were clearly distinguishable. Based on the TEM images of Fe_3O_4@TiO_2@ZIF-8 particles, the average diameter size of Fe_3O_4@TiO_2@ZIF-8 particles was about 400nm.

Figure 2a showed UV/vis spectra of DNM, Fe_3O_4@TiO_2@ZIF-8 NPs, and Fe_3O_4@TiO_2@ZIF-8-DNM NPs. It could be observed that the characteristic UV/vis absorption peaks of DNM were found at 480 nm on the spectrum of Fe_3O_4@TiO_2@ZIF-8-DNM NPs [34], which suggested that DNM was have been grafted by amide reaction. Successful hybridization between Fe_3O_4@TiO_2 NPs and Fe_3O_4@TiO_2@ZIF-8 NPs was also confirmed by FTIR spectroscopy (Figure 2b). The absorption bands in the 1100-1400 cm^{-1} region were ascribed to the C-N stretching of ZIF-8. The peak at 1100 cm^{-1} is attributed to stretching vibration of the C-C. The Fe-O group was detected through the presence of the peak at approximately 590 cm^{-1}. Deformation of O-H band is observed at 1410 cm^{-1}. The peaks at 3410 cm^{-1} indicated the hydroxyl groups of Fe_3O_4@TiO_2@ZIF-8 NPs. These hydrophilic groups on the surface of Fe_3O_4@TiO_2@ZIF-8 NPs could weaken their clearance by the reticuloendothelial system (RES) and prolong their circulation time in blood [35]. Figure 2c shows Zeta potentials of Fe_3O_4, Fe_3O_4@TiO_2 and Fe_3O_4@TiO_2@ZIF-8 nanospheres, which varies from -31.8 ± 1.5 to -33.35 ± 3.65, and 7.04 ± 1.08, respectively. The change from negative charge to positive charge can indicate that ZFI-8 has been modified to Fe_3O_4@TiO_2 NPs. The DLS analysis (Figure 2d) showed that Fe_3O_4@TiO_2 NPs had a mean diameter of 387 nm. Furthermore the coating of Fe3O4@TiO2 NPs with ZIF-8 (Figure 2e) resulted in a slight size increase to 547 nm. DLS analysis of Fe_3O_4@TiO_2 Nps and Fe_3O_4@TiO_2@ZIF-8 Nps showed polydispersity of 0.205 ± 0.09 and 0.374 ± 0.028, respectively. This result indicates that Fe_3O_4@TiO_2 Nps and Fe_3O_4@TiO_2@ZIF-8 Nps with a good dispersion.

Loading and entrapment efficiency

With the large specific surface area, Fe_3O_4@TiO_2@ZIF-8 NPs is supposed to has excellent loading and entrapment behavior. The loading efficiency and entrapment efficiency of the nanocarrier were calculated by measuring the concentration of unbound drug using the absorbance at 490 nm. As shown in figure 3a, Fe_3O_4@TiO_2@ZIF-8 solutions were mixed with DNM at serial concentration ranged from 0.14 to 0.86 mg/mL. It was found that the loading capacity increased as the DNM feeding concentration increasing in 0.2 mg/mL to 0.3 mg/mL. However, the loading capacity reduced suddenly as the DNM feeding concentration increasing in 0.4 mg/mL, this may be due to saturation of the loading capacity. The influence of DNM concentration on the loading capacity became less obvious when the concentration fell in the region from 0.4 mg/mL to 0.6 mg/mL. The concentration of 0.3 mg/mL was thus used for drug loading. The DNM loading capacity increased linearly with the increasing of the initial DNM concentration. As shown in figure 3b, the entrapment efficiency reduce as the DNM feeding concentration increasing in 0.2 mg/mL to 0.6 mg/mL, this is probably due to the gradual reduction in drug loading.

In vitro pH-responsive release

The cumulative drug release experiments were carried out at two different conditions to evaluate the stimuli-response behavior of the Fe_3O_4@TiO_2@ZIF-8 NPs toward pH, the drug releasing was investigated at pH 5.6 and 7.4, which is close to the tumor and physiological microenvironment respectively [36,37]. As shown in figure 4, DNM was released very slowly from the nanocarrier at neutral conditions (pH 7.4). There was only about 14.3% of the total bound released for 96 h. While when pH decreased, the release efficiency of DNM enhanced evidently. After 96 h, nearly 79.01% of the total DNM was released from the nanocarrier under the pH of tumor tissues (pH 5.6). Especially between 1 and 24 h, DNM released significantly faster under pH 5.6 compare with pH 7.4 conditions. As such, the prepared Fe_3O_4@TiO_2@ZIF-8-DNM NPs may be further developed as a pH-responsive release system that can target tumor cells and allow drug release within acidic intracellular compartments such as endosome and lysosome, where the pH value is lower than that in the normal tissue.

Cytotoxicity of Fe_3O_4@TiO_2@ZIF-8 NPs

Biocompatibility is an important factor for anti-cancer drug delivery. Here we performed MTT assays to test the toxicity of

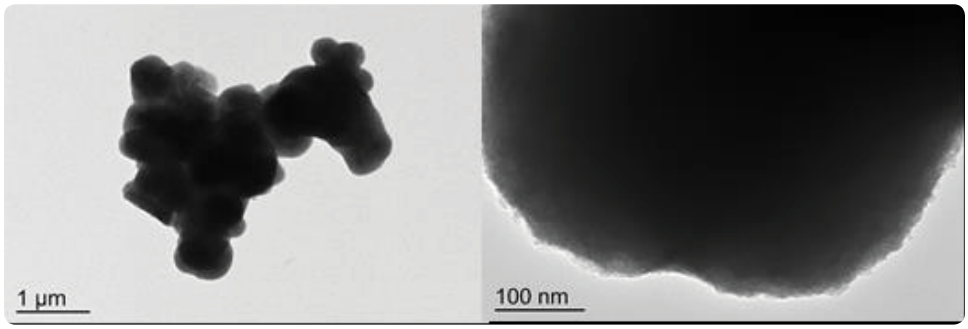

Figure 1: TEM image of Fe_3O_4@TiO_2@ZIF-8 NPs.

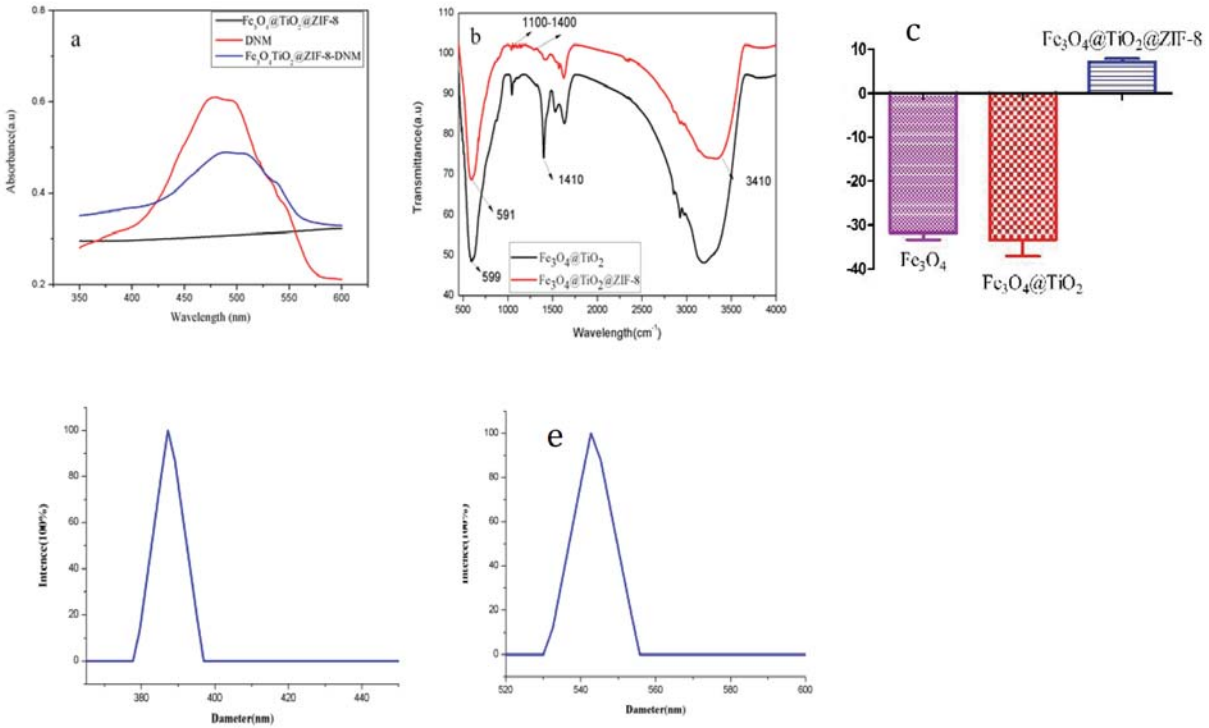

Figure 2: **a.** UV−vis absorption; **b.** FTIR spectra of Fe_3O_4@TiO_2 and Fe_3O_4@TiO_2@ZIF-8 NPs; **c.** Zeta potentials of Fe_3O_4, Fe_3O_4@TiO_2 and Fe_3O_4@TiO_2@ZIF-8 nanospheres; **d.** Fe_3O_4@TiO_2 NPs; **e.** Fe_3O_4@TiO_2@ZIF-8 NPs size DLS analysis

Fe_3O_4@TiO_2@ZIF-8 NPs with a dose dependent. MTT assay was a general quantified data to describe the cytotoxicities of biomaterials (Fe_3O_4@TiO_2@ZIF-8) towards the cells they incubated [38]. As showed in figure 5, from the highest to the lowest concentration of Fe_3O_4@TiO_2@ZIF-8 NPs incubated with cells, there was no noticeable differences of cell viabilities observed. And the viabilities of HeLa cells were over 90% at all test concentrations after incubated with Fe_3O_4@TiO_2@ZIF-8 NPs. This result showed that Fe_3O_4@TiO_2@ZIF-8 NPs were biocompatible and could be used as drug delivery among intracellular experiments.

Magnetic targeting study

The magnetic properties of the nanocarrier with and without magnetite nanoparticles-loaded were investigated in our previous report [39], and both of them exhibited good superparamagnetism. Therefore, we carried out an in vitro magnetic targeting experiment to examine the potential application of the nanoplatform for magnetic drug targeting in figure 6. After incubation, in the magnetic region (red circle), Many cells have a round shape with no fixed form in the cell culture media. This was the significant signal of cell death. However, for the control region where the magnetic field was much weaker (blue circle), the cells suffered much less death than the magnetic position. The result demonstrated that the magnetic nanospheres exposed to a magnetic field could rapidly accumulate in the targeting area. The external magnetic field can significantly increase the local concentration of magnetic nanospheres, which implies that the magnetic nanospheres could efficiently accumulate to the tumor under a magnetic guidance.

Cellular uptake and endocytosis of the magnetic nanospheres

To detect the presence of the Fe_3O_4@TiO_2@ZIF-8-DNM NPs nanospheres in HeLa cells, intracellular "Fe" was stained by Prussian blue. In the absence of Fe_3O_4@TiO_2@ZIF-8-DNM nanospheres,

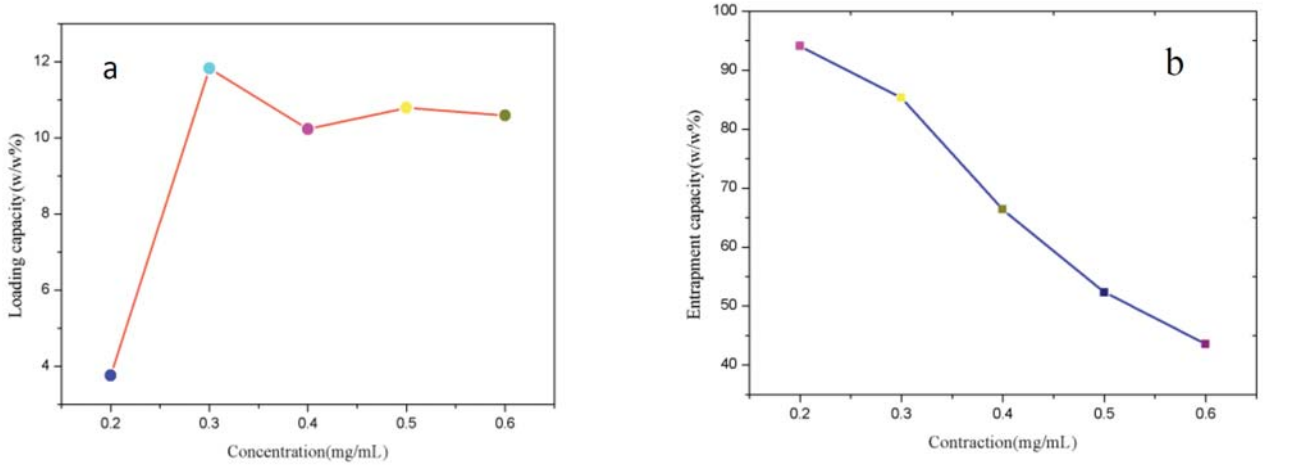

Figure 3: DNM loading efficiency. **a**. Entrapment efficiency; **b**. Results under different DNM concentration.

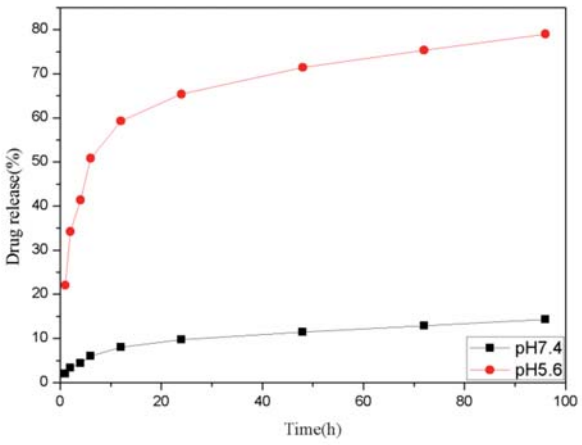

Figure 4: *In vitro* DNM release behaviors at pH 7.4 and 5.6, respectively.

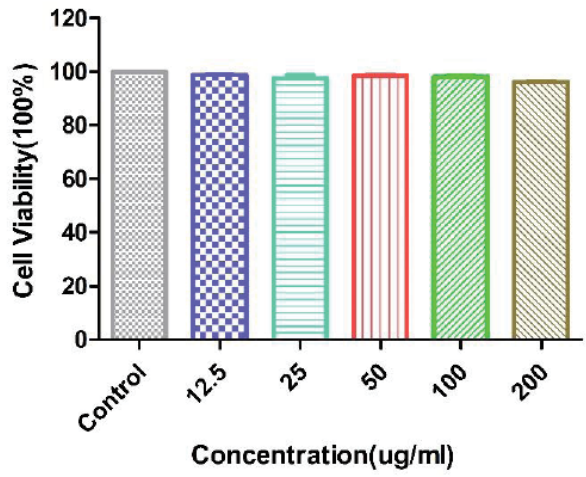

Figure 5: HeLa cell viability under different concentrations of Fe_3O_4@TiO_2@ ZIF-8NPs.

negligible blue staining was observed for the control cells (Figure 7a). However, after the incubation with the Fe_3O_4@TiO_2@ZIF-8-DNM NPs, substantial blue spots were observed in most of the cells (Figure 7b). The majority of the blue spots seem to be localized inside the cells, indicating high cellular internalization of the magnetic nanospheres [40].

Then, flow cytometry analysis was performed to compare endocytosis of Fe_3O_4@TiO_2@ZIF-8-DNM NPs and free DNM using HeLa cells. Since DNM itself is fluorescent, it was used directly to measure cellular uptake without additional markers. Therefore, the fluorescence intensity is pro-portional to the amount of DNM internalized by the cells. As shown in figure 8, Cells without any DNM treatment were used as a negative control and showed only the autofluorescence of the cells. When the cells were treated with DNM or Fe_3O_4@TiO_2@ZIF-8-DNM NPs, the signals in the cells were obviously increased. Both free DNM and Fe_3O_4@TiO_2@ZIF-8-DNM NPs were taken by cells; however, the uptake efficiency was greatly different. After 24 h of incubation, the amount of cellular uptake of Fe_3O_4@TiO_2@ZIF-8-DNM (MFI=148) was approximately twice that of DNM (MFI = 79). This phenomenon may due to the charge-reversal nanocarrier can be selectively internalized into the targeted.

To further explore the difference in uptake of drug-nanostructure systems by Hela cells, we tracked DNM internalization into the cells through the colocalization of the DNM signal (red fluorescence). Since DNM has red fluorescence, its distribution in the Hela cells can be easily observed under a fluorescence microscope. As shown in figure 9, cells exposed to Fe_3O_4 @ TiO_2 @ ZIF-8-DNM NPs showed higher DNM fluorescence intensity in cells after 12 h of incubation. In the case of free DNM, the intensity of red fluorescence was mainly observed in cells, indicating that DNM-conjugated nanoparticles can be targeted to accumulate in cancer cells and have good drug delivery in cells.

Inhibition of cell migration

In order to determine whether the cell migration and invasion were influenced by the treatment of Fe_3O_4@TiO_2@ZIF-8-DNM NPs, scratch wound assay were carried out. As is shown in figure 10, Fe_3O_4@TiO_2@ZIF-8-DNM NPs significantly decreased the repair rate of wound by the four fold compared to control. Moreover, our results

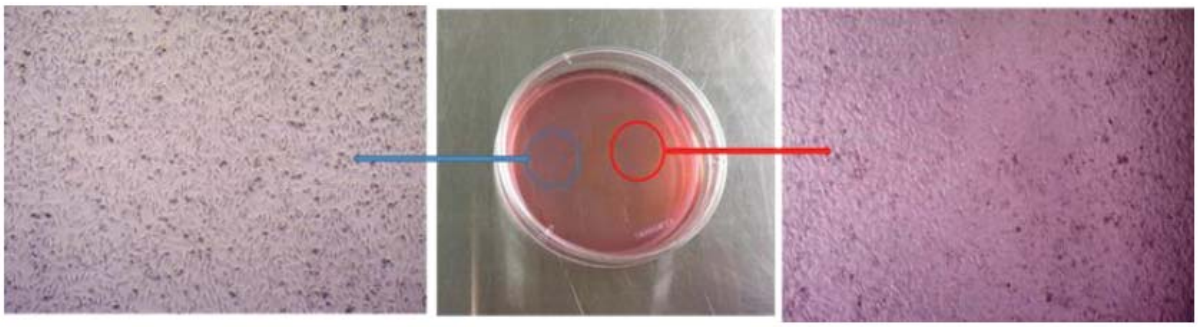

Figure 6: Optical micrographs of HeLa cells at the targeting area (red circle) and the control area (blue circle) after incubating with Fe_3O_4@TiO_2@ZIF-8-DNM NPs (50μg/ ml) for 6h under an external magnetic field (about 4 T).

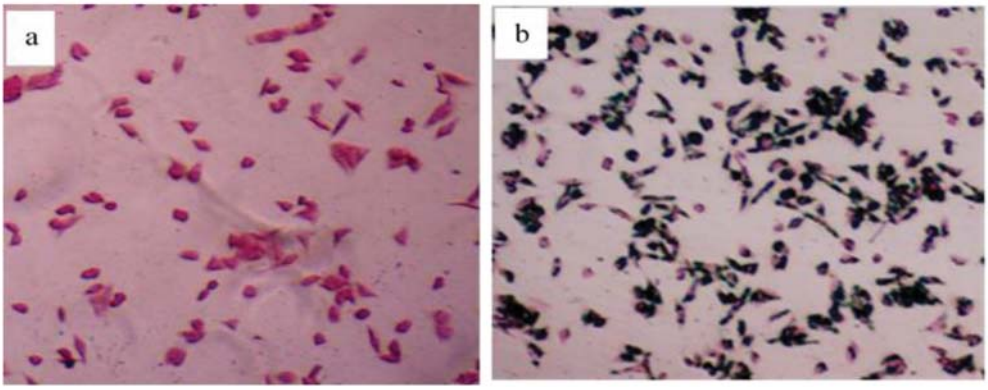

Figure 7: Prussian blue staining of HeLa cells treated in the absence and presence of the Fe_3O_4@TiO_2@ZIF-8 magnetic nanospheres (50μg/ ml) for 6h.

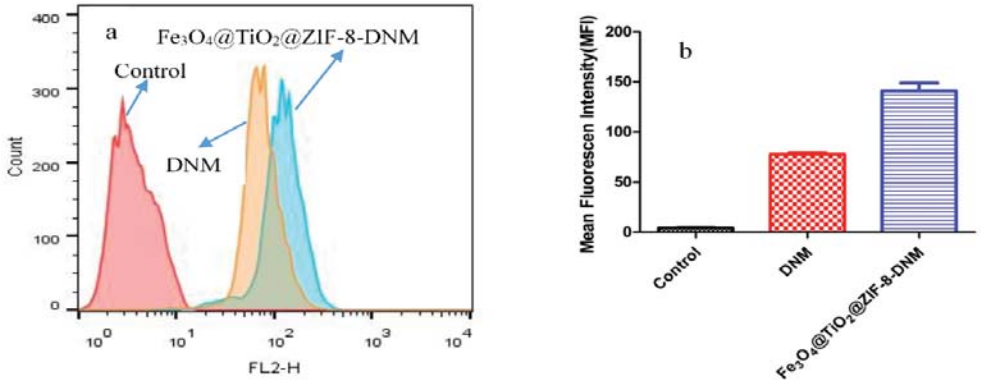

Figure 8: Fe_3O_4@TiO_2@ZIF-8-DNM NPs delivery efficiency to Hela cells. **a.** Representative histograms of DNM in different nanospheres. **b**. MFI flow cytometry analysis to HeLa cells.

showed that the minimal fraction of HeLa cells not committed to cell death did not display any capacity of closing wounds after incubation with the nanospheres.

Evaluation of cell cycle arrest and apoptosis from Fe_3O_4@ TiO_2@ZIF-8-DNM NPs

The effect of Fe_3O_4@TiO_2@ZIF-8-DNM NPs and DNM on the cell cycle and apoptosis was investigated by flow cytometry. As shown in figure 11, the FACS results showed the presence of early apoptotic, advanced apoptotic and necrotic cell populations in treated Hela cells. The fractions of cells that was in early apoptosis were positive for Annexin and was placed in the lower right quadrant. The FACS results demonstrated that Fe_3O_4@TiO_2@ZIF-8-DNM NPs treated Hela cells showed greater numbers of cells in early apoptosis, i.e. 10.6% compared with 6.20% for free DNM treated Hela cells. This result suggested that cells treated with Fe_3O_4@TiO_2@ZIF-8-DNM NPs were able to induce greater apoptosis in the Hela cell line in comparison with the free DNM. FACS results suggested that Fe_3O_4@ TiO_2@ZIF-8 NPs had little cytotoxicity and it may be due to the coating of ZIF-8.

To further define the mechanism of the antiproliferative effect of the Fe_3O_4@TiO_2@ZIF-8-DNM NPs on tumor cells, the cell cycle of

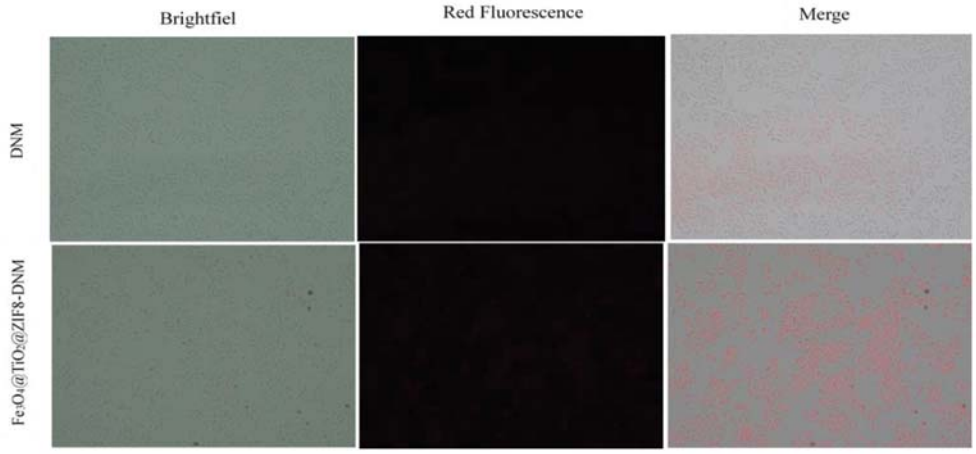

Figure 9: The cell internalization of DNM and Fe_3O_4@TiO_2@ZIF-8-DNM assessed by fluorescence microscope.

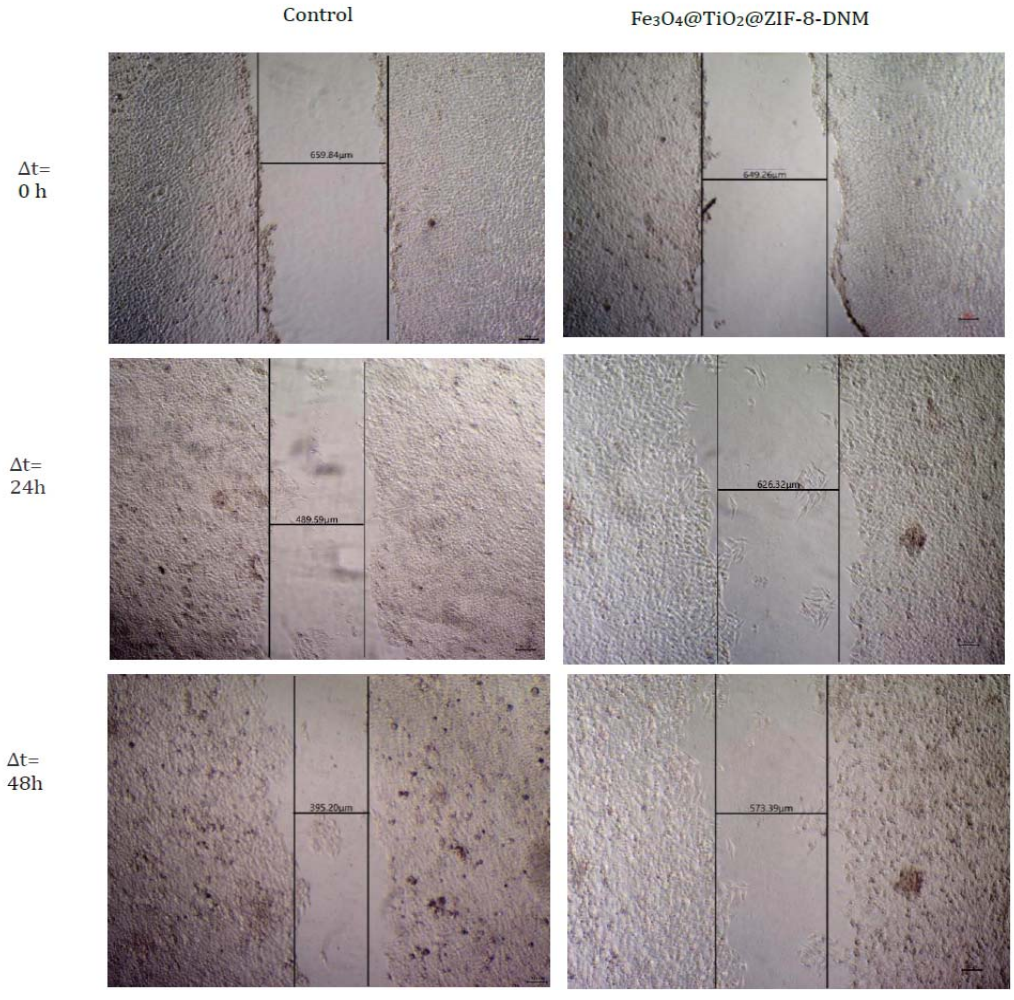

Figure 10: Analysis of cell migration for control and cells incubated with Fe_3O_4@TiO_2@ZIF-8-DNM NPs for 0 h, 24h, and 48h by scratch wound assay.

HeLa cells was studied by flow cytometry in Propidium Iodide (PI)-stained cells after treatment with Fe_3O_4@TiO_2@ZIF-8-DNM NPs for 24 h. The cell statuses were given in figure 12, in which the cell cycles in the presence of DNM was also given for better understanding of the mechanism.

Compared with the control, there were significant increased G2/M phases distributions in the cell cycles for the cells treated with DNM or Fe_3O_4@TiO_2@ZIF-8-DNM NPs. Since the G2/M phases represent the DNA synthetic period of the cancer cells, the enhanced distribution in these phases indicated that the antiproliferative

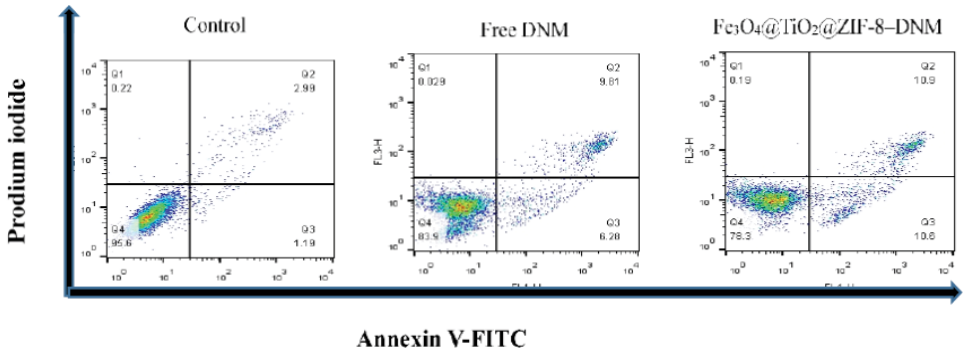

Figure 11: Flow cytometry data for HeLa cells after incubation of Fe_3O_4@TiO_2@ZIF-8 DNM and Fe_3O_4@TiO_2@ZIF-8-DNM for 24 h, respectively. The cells are stained with Annexin V-FITC and PI. Dot plots of FITC-labeled Annexin V (horizontal axis) and PI fluorescence (vertical axis) are shown with the logarithmic fluorescence intensity. Quadrants: lower left, live cells; lower right, early apoptotic cells; upper right, late apoptotic cells; upper left, dead (necrotic) cells.

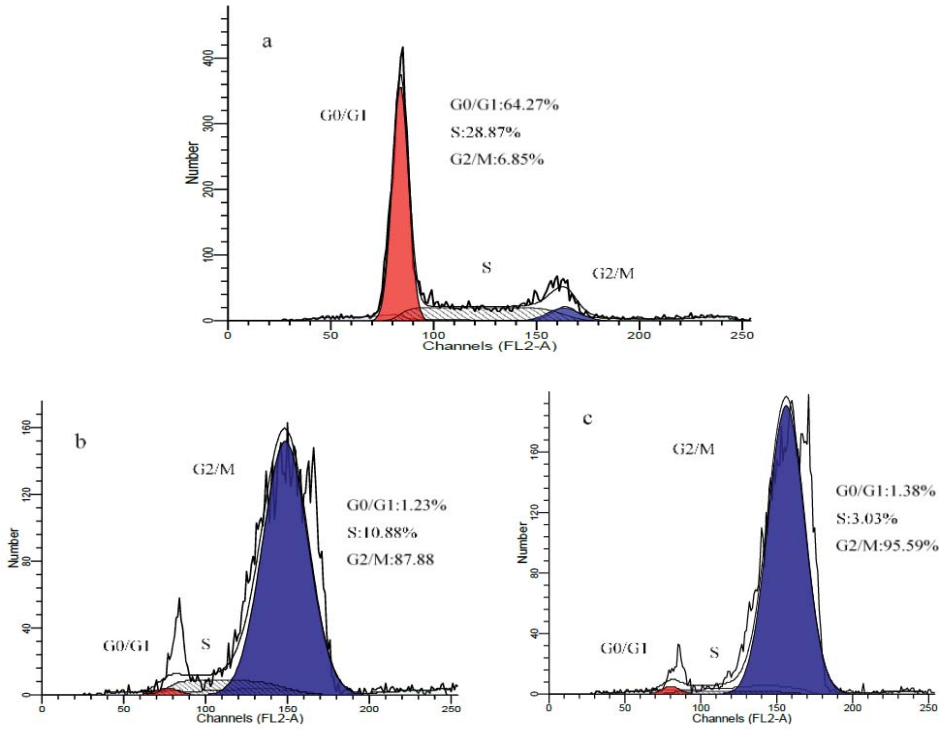

Figure 12: Cell cycle status of the HeLa cell line after treatment with Fe_3O_4@TiO_2@ZIF-8-DNM NPs and free DNM for 24h.

mechanism induced by the inhibition of DNA duplication. This result was in high consistent with the well-known conclusion that DNM induced the apoptotic of cancer cells by inserting DNA duplex structures with its plat anthraquinone rings [41-43]. The similar change for Fe_3O_4@TiO_2@ZIF-8-DNM NPs indicated that the drug loading process did not influence the anti-cancer activity of DNM. The mechanism of cell apoptosis was investigated by the following fluorescence staining and flow cytometry methods.

Anticancer activity study

As observed by MTT assay Fe_3O_4@TiO_2@ZIF-8-DNM NPs induced toxicity on both the cells types due to the action of the loaded DNM as shown in figure 13. However, DNM loaded nanoparticles caused more toxicity to the HeLa cells than the A549 cells. 0.25 µg/mL of Fe_3O_4@TiO_2@ZIF-8-DNM NPs induced 30% death of the A549 cells whereas the same amount of Fe_3O_4@TiO_2@ZIF-8-DNM NPs caused 48% death of the HeLa cells. Again, upon treatment with 1 µg/mL of Fe_3O_4@TiO_2@ZIF-8-DNM NPs (µg/mL), 85% HeLa cell death was observed in contrast to only 44% A549 cells cell death. Therefore, from cell viability assay it can be elucidated that Fe_3O_4@TiO_2@ZIF-8-DNM induced more toxicity to Hela cells than A549 cells. In addition, the cytotoxicity of Fe_3O_4@TiO_2@ZIF-8-DNM NPs was higher than that of free DNM after 48 h incubation, which could be explained by the difference in cellular uptake routes between Fe_3O_4@TiO_2@ZIF-8-DNM NPs and free DNM. The Fe_3O_4@TiO_2@ZIF-8-DNM NPs were taken up efficiently and accumulated in tumor cells via endocytosis, and consequently killed the cells at enhanced efficacy, whereas the free DNM entered the cancer cells just through molecule diffusion.

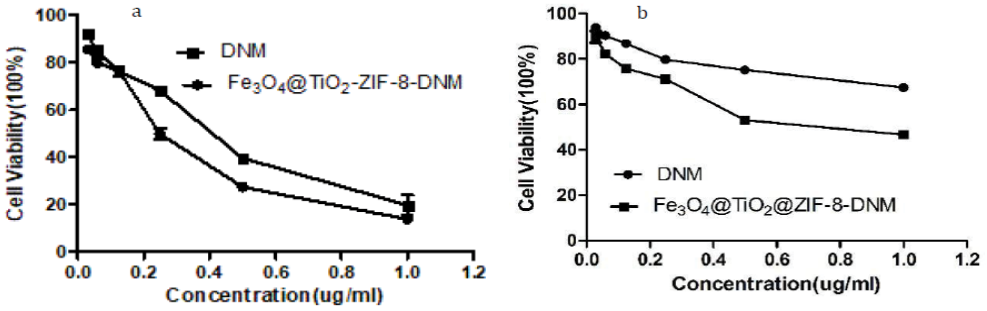

Figure 13: Cytotoxicity of Fe_3O_4@TiO_2@ZIF-8-DNM and pure DNM toward tumor cells (a) HeLa, and (b) A549, respectively, from MTT assays.

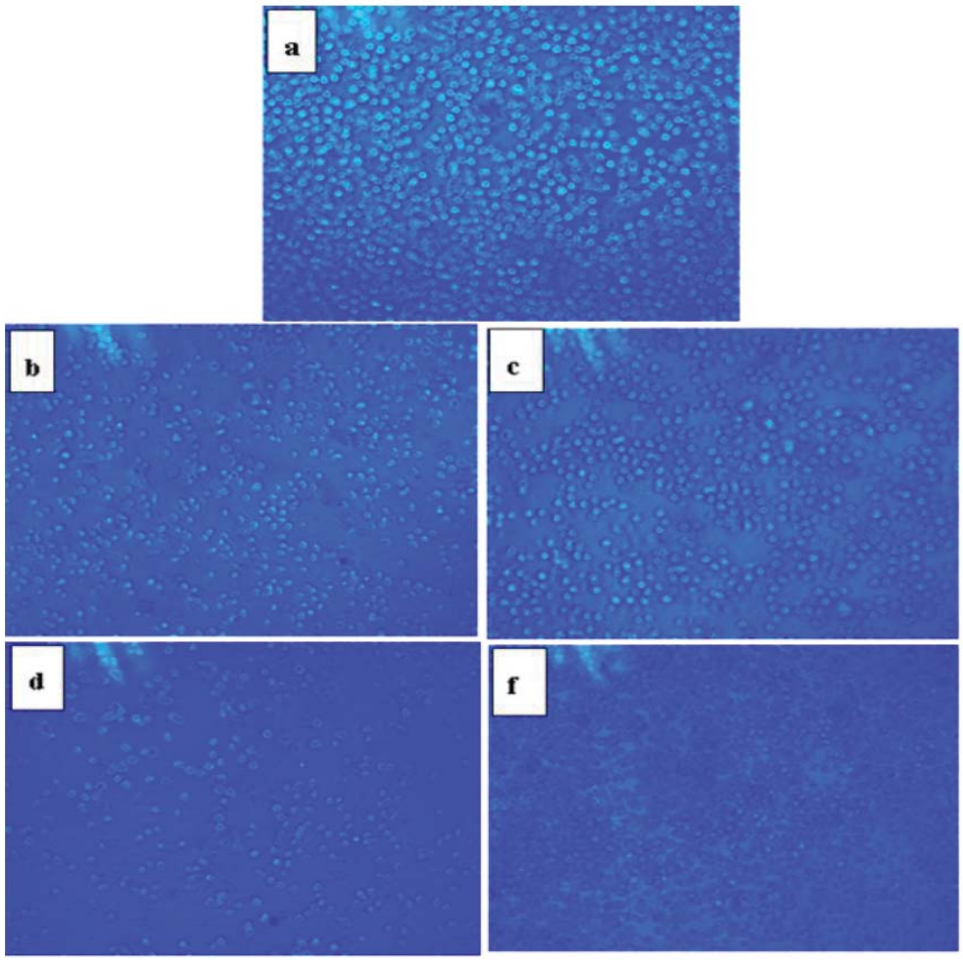

Figure 14: Relative cellular viability of Hela cells against Fe_3O_4@TiO_2@ZIF-8 (a), free DMN (b,d) and Fe_3O_4@TiO_2@ZIF-8-DNM(c,f) in 0.5 and 1μg/ mL concentration of typical experiment respectively.

Using Trypan blue assay, we can observed more intuitively the number of live cells under treatments with different concentrations of Fe_3O_4@TiO_2@ZIF-8-DNM NPs and free DNM for 24 h (Figure 14). Results of Trypan blue assay showed that Fe_3O_4@TiO_2@ZIF-8-DNM NPs at 1 μg/mL dosage significantly resulted in death of HeLa cells which was also in accordance with the findings obtained from the MTT assay. Direct observation of trypan blue changes to the HeLa cells after exposing them to different drug formulations (with DNM concentrations of 0.5 and 1 μg/mL, respectively) also confirmed that the Fe_3O_4@TiO_2@ZIF-8-DNM NPs was as effective as free DNM in inhibiting the growth of all of the three tested cancer cell lines.

CONCLUSIONS

In summary, we successfully fabricated the core-shell structured Fe_3O_4@TiO_2@ZIF-8 nanoparticles, which could deliver DNM to tumor regions for combined pH-responsbile and magnetic targeted

therapy. Our results demonstrated that in vitro tumor therapy with significant inhibition efficacy for tumor growth was achieved using DNM-loaded MOF-based Fe_3O_4@TiO_2 nanocarriers. The Fe_3O_4@TiO_2@ZIF-8 NPs exhibited more relevant and satisfactory properties such as improved drug loading content, good biocompatibility, effective cellular uptake and more sensitive, pH-triggered drug release behavior as drug delivery vehicles from in vitro experiments. It was also demonstrated that the hybrid nanoparticles could inhibit tumor growth effectively compared with free DNM in the cancer cells. More efforts for designing pH-sensitive MOFs should be directed to the combination of high drug-loading capacity and multifunctional imaging based on well-established biocompatible materials in the future. The cumulative drug release experiments show that Fe_3O_4@TiO_2@ZIF-8-DNM NPs could retain for a long time at pH 5.6, which was helpful to minimize the adverse effect and enhance the therapeutic effect. In vitro experiments, better anticancer activity was observed in Fe_3O_4@TiO_2@ZIF-8-DNM NPs therapy group, indicating the potential of Fe_3O_4@TiO_2@ZIF-8-DNM NPs for cancer therapy.

ACKNOWLEDGEMENTS

The author(s) disclosed receipt of the following financial support for the research, authorship, and/or publication of this article: This work was financially supported by the Natural Science Foundation of Guangdong (2016A030313807) and the Outstanding Young Teachers' Foundation in Colleges and Universities of Guangdong Province the Wenzhou Medical University and Wenzhou Institute of Biomaterials & Engineering (WIBEZD2017001-03).

REFERENCES

1. Zarogoulidis P, Chatzaki E, Porpodis K, Domvri K, Hohenforst SW, Goldberg EP, et al. Inhaled chemotherapy in lung cancer: future concept of nanomedicine. Int J Nanomedicine. 2012; 7: 1551-1572. https://goo.gl/J6jusz
2. Jaracz S, Chen J, Kuznetsova LV, Olima I. Recent advances in tumor-targeting anticancer drug conjugates. Bioorg Med Chem. 2005; 13: 5043-5054. https://goo.gl/1grgtq
3. Primeau A J, Rendon A, Hedley D, Lilge L, Tannock IF. The distribution of the anticancer drug Doxorubicin in relation to blood vessels in solid tumors. Clin Cancer Res. 2005; 11: 8782-8788. https://goo.gl/RqeME6
4. Chang YL, Liu N, Chen L, Xinlei M, Yanjing L, Yapeng L, et al. Synthesis and characterizatio of DOX-conjugated dendrimer-modified magnetic iron oxide conjugates for magnetic resonance imaging, targeting, and drug delivery. Journal of Materials Chemistry. 2012; 19: 9594-9601. https://goo.gl/oQNXHX
5. Shen S, Wu L, Liu J, Xie M, Shen H, Qi X, et al. Core-shell structured Fe_3O_4@TiO_2-doxorubicin nanoparticles for targeted chemo-sonodynamic therapy of cancer. International Journal of Pharmaceutics. 2015; 486: 380-388. https://goo.gl/2Pqu85
6. Kievit FM, Wang FY, Fang C, Mok H, Wang K, Silber JR, et al. Doxorubicin loaded iron oxide nanoparticles overcome multidrug resistance in cancer *In vitro*. J Control Release. 2011; 152: 76-83. https://goo.gl/uJsqpp
7. Verma VK, Kamaraju SR, Kancherla R, Kona LK, Beevi SS, Debnath T, et al. Fluorescent magnetic iron oxide nanoparticles for cardiac precursor cell selection from stromal vascular fraction and optimization for magnetic resonance imaging. Int J Nanomedicine. 2015; 10: 711-726. https://goo.gl/QmnbtL
8. Zhao X, Zhao H, Yuan H, Lan Minbo. Multifunctional superparamagnetic Fe_3O_4@SiO_2core/shell nanoparticles: design and application for cell imaging. Journal of Biomedical Nanotechnology. 2014; 10: 262-270. https://goo.gl/tkeotF
9. Shang L, Wang Q, Chen K, Jing Q, Qing HZ, Jian BL, et al. SPIONs/DOX loaded polymer nanoparticles for MRI detection and efficient cell targeting drug delivery. Rsc Advances. 2017; 7: 47715-47725. https://goo.gl/5Wi8kR
10. Vyas D, Lopezhisijos N, Gandhi S, El-Dakdouki M, Basson MD, Walsh MF, et al. Doxorubicin-Hyaluronan Conjugated Super-Paramagnetic Iron Oxide Nanoparticles (DOX-HA-SPION) enhanced cytoplasmic uptake of doxorubicin and modulated apoptosis, IL-6 Release and NF-kappaB activity in human MDA-MB-231 breast cancer cells. J Nanosci Nanotechnol. 2015; 15: 6413-6422. https://goo.gl/UCRRKB
11. Zolata H, Afarideh H, Abbasi DF. Radio-immunoconjugated, Dox-loaded, surface-modified Superparamagnetic Iron Oxide Nanoparticles (SPIONs) as a bioprobe for breast cancer tumor theranostics. Journal of Radioanalytical & Nuclear Chemistry. 2014; 301: 451-460. https://goo.gl/8y1J6P
12. Ma WF, Zhang Y, Li LL, Li JY, Peng Z, Yu TZ, et al. Tailor-made magnetic Fe_3O_4@$mTiO_2$ microspheres with a tunable mesoporous anatase shell for highly selective and effective enrichment of phosphopeptides. Acs Nano. 2012; 6: 3179-3188. https://goo.gl/CAM1bM
13. Zeng L, Ren W, Xiang L, Jianjun Z, Bin C, Aiguo W. Multifunctional Fe_3O_4-TiO_2 nanocomposites for magnetic resonance imaging and potential photodynamic therapy. Nanoscale. 2013; 5: 2107-2113. https://goo.gl/XoW1Nw
14. Liu MC, Liu B, Sun XY, Lin HC, Lu JZ, Jin SF, et al. Core/Shell structured Fe_3O_4@TiO_2-DNM nanospheres as multifunctional anticancer platform: Chemotherapy and photodynamic therapy research. Journal of Nanoscience & Nanotechnology. 2018; 18: 4445-4456. https://goo.gl/s35Zx2
15. Rowsell JLC, Yaghi OM. Strategies for hydrogen storage in metal-organic frameworks. Angewandte Chemie International Edition. 2005; 44: 4670-4679. https://goo.gl/yGw8n4
16. Mircea Dinca, Jeffrey R. Long Hydrogen storage in microporous metal-organic frameworks with exposed metal sites. Angewandte Chemie. 2008; 47: 6766-6779. https://goo.gl/rmbjLz
17. Banglin C, Shengqian M, Eric JH, Emil BL, Chengdu L, Haoguo Z, et al. Selective gas sorption within a dynamic metal-organic framework. Inorganic Chemistry. 2007; 46: 8705-8709. https://goo.gl/zrPqp3
18. Chen B, Yang Y, Zapata F, Lin G, Qian G, Lobkovsky EB. Luminescent open metal sites within a metal-organic framework for sensing small molecules. Advanced Materials. 2010; 19: 1693-1696. https://goo.gl/A4kQZE
19. Jiang HL, Tatsu Y, Lu ZH, Qiang Xu. Non-, Micro-, and mesoporous metal-organic framework isomers: Reversible transformation, fluorescence sensing, and large molecule separation. Journal of the American Chemical Society. 2010; 132: 5586-5587. https://goo.gl/cwiYK2
20. Cui Y, Li B, He H, Wei Z, Banglin C, Guodong Q. Metal-organic frameworks as platforms for functional materials. Acc Chem Res. 2016; 49: 483-493. https://goo.gl/Uti5jv
21. Lee JY, Farha OK, Roberts J, Karl AS, SonBinh TN, Joseph TH. Metal-organic framework materials as catalysts. Chem Soc Rev. 2009; 38: 1450-1459. https://goo.gl/v5aKg1
22. Kuo CH, Tang Y, Chou LY, Brian TS, Casey NB, Zipeng Z, et al. Yolk-shell nanocrystal@ZIF-8 nanostructures for gas-phase heterogeneous catalysis with selectivity control. Journal of the American Chemical Society. 2012; 134: 14345. https://goo.gl/NTrUrj
23. Liu RL, Yu P, Zhimin L, Qiang Fu. Multicolor fluorescent carbon nanodots@ zeolitic imidazolate framework-8 nanoparticles for simultaneous pH-responsive drug delivery and fluorescence imaging. Journal of Controlled Release. 2017; 259: 118-119. https://goo.gl/EnyrAD
24. Horcajada P, Chalati T, Serre C, Brigitte G, Catherine S, Tarek B, et al. Porous metal-organic-framework nanoscale carriers as a potential platform for drug delivery and imaging. Nature Materials. 2010; 9: 172-178. https://goo.gl/go3LW4
25. Sun CY, Qin C, Wang XL, Guang SY, Kui ZS, Ya QL. Zeolitic imidazolate framework-8 as efficient pH-sensitive drug delivery vehicle. Dalton Transactions. 2012; 41: 6906-6909. https://goo.gl/xkpCja
26. Grabe M, Oster G. Regulation of organelle acidity. J Gen Physiol. 2001; 117: 329-344. https://goo.gl/4Uq1yw
27. Zhuang J, Kuo CH, Chou LY, Liu DY, Weerapana E, Tsung CK. Optimized metal-organic-framework nanospheres for drug delivery: evaluation of small-molecule encapsulation. Acs Nano. 2014; 8: 2812-2819. https://goo.gl/X6qNZF
28. Miralda CM, Macias EE, Zhu M, Ratnasamy P, Carreon MA. Zeolitic Imidazole Framework-8 Catalysts in the Conversion of CO2 to Chloropropene Carbonate. ACS Catal. 2012; 2: 180-183. https://goo.gl/pFvX1s

29. Wu YN, Zhou M, Li S, Zehua Li, Jie Li, Baozhen Wu, et al. Magnetic metal-organic frameworks: γ-Fe_2O_3@MOFs *via* confined *In situ* pyrolysis method for drug delivery. Small. 2014; 10: 2927-2936. https://goo.gl/SHV9NX

30. Chen WJ, Tsai PJ, Chen YC. Functional Fe_3O_4/TiO_2 core/shell magnetic nanoparticles as photokilling agents for pathogenic bacteria. Small. 2008; 4: 485-491. https://goo.gl/JD1jU4

31. Liang X, Gao C, Cui L, Wang S, Wang J, Dai Z. Self-assembly of an Amphiphilic Janus camptothecin-floxuridine conjugate into liposome-Like nanocapsules for more efficacious combination chemotherapy in cancer. Advanced Materials. 2017; 29: 1703135-1703144. https://goo.gl/5xwgmV

32. Moreira AF, Gaspar VM, Costa EC, de Melo-Diogo D, Machado P, Paquete CM, et al. Preparation of end-capped pH-sensitive mesoporous silica nanocarriers for on-demand drug delivery. European Journal of Pharmaceutics & Biopharmaceutics. 2014; 88: 1012-1025. https://goo.gl/GffG9z

33. Yoo H, Park J, Kwon S. *In vitro* cytotoxic activity of some Korean medicinal plants on human cancer cell lines: enhncement in cytotoxicoty by heat processing. Phytotherapy Research. 2010; 21: 900-903. https://goo.gl/ADe8Kr

34. Shi J, Liu Y, Wang L, Gao J, Zhang J, Yu X, et al. A tumoral acidic pH-responsive drug delivery system based on a novel photosensitizer (fullerene) for in vitro and in vivo chemo-photodynamic therapy. Acta Biomater. 2014; 10: 1280-1291. https://goo.gl/oU7Cwq

35. Barbé C, Bartlett J, Kong L, Finnie K, Lin HQ, Larkinet M, et al. Silica particles: A Novel drug delivery system. Advanced Materials. 2010; 16: 1959-1966. https://goo.gl/ShHBmN

36. Sahoo B, Devi KS, Dutta S, Maiti TK, Pramanik P, Dhara D. Biocompatible mesoporous silica-coated superparamagnetic manganese ferrite nanoparticles for targeted drug delivery and MR imaging applications. J Colloid Interface Sci. 2014; 431: 31-41. https://goo.gl/m8YBEX

37. Moreira A F, Gaspar V M, Costa E C, et al. Preparation of end-capped pH-sensitive mesoporous silica nanocarriers for on-demand drug delivery. Eur J Pharm Biopharm. 2014; 88: 1012-1025. https://goo.gl/ri11oE

38. Li S, Wang K, Shi Y, Yanan C, Binlong C, Bing H, et al. Novel biological functions of ZIF-NP as a delivery vehicle: High pulmonary accumulation, favorable biocompatibility, and improved therapeutic outcome. Advanced Functional Materials. 2016; 26: 2715-2727. https://goo.gl/drxqRb

39. Ding G, Guo Y, Lv Y, Liu X, Xu L, Zhang X. A double-targeted magnetic nanocarrier with potential application in hydrophobic drug delivery. Colloids & Surfaces B Biointerfaces. 2012; 91: 68-76. https://goo.gl/NngQFn

40. Zeng L, Ren W, Zheng J, Aiguo W, Ping C. Synthesis of water-soluble FeOOH nanospindles and their performance for magnetic resonance imaging. Applied Surface Science. 2012; 258: 2570-2575. https://goo.gl/zC6tx6

41. Munnier E, Cohen JS, Herve K, Linassier C, Souce M, Dubois P, et al. Doxorubicin delivered to MCF-7 cancer cells by superparamagnetic iron oxide nanoparticles: effects on subcellular distribution and cytotoxicity. Journal of Nanoparticle Research. 2011; 13: 959-971. https://goo.gl/iTLrQ5

42. Doughty B, Rao Y, Kazer SW, Sheldon JJ Kwok, Nicholas JT, Kenneth BE. Binding of the Anti-cancer drug daunomycin to DNA probed by second harmonic generation. Journal of Physical Chemistry B. 2013; 117: 15285-15289. https://goo.gl/kTxBUX

43. Zhao P, Lu JZ, He J, Chen WH, Chen PP, Chen DW, et al. Synthesis, DNA-binding, and photocleavage properties of a serious of porphyrin-daunomycin hybrids. Nucleosides & Nucleotides. 2014; 33: 597-614. https://goo.gl/SVvPdz